Solid Oxide Iron-Air Battery for Long-Duration Energy Storage: A Study on Reduction Kinetics of Energy Storage Material Fe-ZrO_2 Catalyzed by Ir Particles

ECS Transactions, 111 (6) 1771-1783 (2023)
10.1149/11106.1771ecst ©The Electrochemical Society

Solid Oxide Iron-Air Battery for Long-Duration Energy Storage: A Study on Reduction Kinetics of Energy Storage Material Fe-ZrO_2 Catalyzed by Ir Particles

Chaitali Morey[a], Qiming Tang[a, b], Kevin Huang[a*]

[a] Department of Mechanical, University of South Carolina, Columbia, South Carolina 29208, USA
[b] Maryland Energy Innovation Institute, University of Maryland, College Park, MD 20742, USA
[a*] Department of Mechanical, University of South Carolina, Columbia, South Carolina 29208, USA

Long duration electricity storage (LDES) with 10+ hour cycle duration is an economically competitive option to accelerate the penetration of renewable energy into the utility market. Unfortunately, none of the available energy storage technologies can meet the LDES' requirements for duration and cost. We here report a focused kinetic study on Fe-oxide reduction process, which is a key step for solid oxide iron-air battery; the latter has been recently demonstrated as a LDES compatible battery. The study clearly shows that Ir is an excellent catalyst to boost the sluggish Fe-oxide reduction kinetics.

1. Introduction

Long duration energy storage (LDES) (10+ hours) is considered a key technical solution for the penetration of renewable energy into the utility market. However, the currently available storage technologies are limited to less than 10 hours for cost reason. The benchmark Li-ion battery technology would be economically prohibitive if the storage time goes beyond 4 hours. Therefore, developing new low-cost LDES-compatible battery technologies is highly desirable.

In recent years, we have been researching on a new type of metal-air battery for LDES applications. The battery is consisted of solid oxide-ion electrolyte and porous electrodes and operated on oxide-ion chemistry. In this battery, the chemical energy of oxygen as transported in the form of O^{2-} by the oxide-ion conductor (electrolyte) is reversibly stored in an energy-dense Fe/FeO_x-bed (or abbreviated as "Fe-bed") that is integrated within the anode chamber of a reversible solid oxide cell (RSOC) [1-4]. During operation, the oxygen electrode (OE) and hydrogen electrode (HE) are open to air of an unlimited oxygen source and enclosed to a low-cost Fe-bed chamber, respectively. Upon cycling, RSOC alternately operates in fuel cell mode during discharge and electrolyzer mode during charge, while the oxygen is being transferred via a gas-phase H_2/H_2O shuttle and stored within the Fe-bed via the Fe-O redox reaction. One unique feature of SOIAB is its free access to oxygen in air (thus no oxygen storage needed for OE), making it suited for LDES applications.

From our early work, we have identified two major problems limiting the overall performance of a solid oxide iron-air battery: 1) sluggish FeO_x-to-Fe reduction kinetics in

the Fe-bed; [5] 2) RSOC's high electrode overpotentials [1]. To address these issues, we have previously shown that synthesis of nanostructured Fe-bed materials [3] and addition of catalyst (*e.g.*, Pd) nanoparticles can boost the FeO_x-to-Fe reduction kinetics [1]. However, our effort to further improve RSOC's electrochemical performance has been very limited until very recently we have demonstrated that adding Ir into Fe-bed can significantly improve the kinetics of FeO_x reduction [6].

To understand the slow kinetic issue, we have also previously measured the rate constant of the H_2 reduction process of FeO_x-ZrO_2 [7, 8]. These kinetic data are very useful for our multiphysics modeling effort. However, there is a lack of similar dataset for Ir-catalyzed FeO_x-ZrO_2 reduction process. Therefore, the goal of this study is to acquire this set of data for comparison with the rate constant of baseline FeO_x-ZrO_2 H_2-reduction and future multiphysics modeling of the battery.

2. Experimental Method

2.1 Material Synthesis

Fe_2O_3-ZrO_2 Baseline: The starting Fe_2O_3/ZrO_2 composite material was prepared by the co-precipitation method. Briefly, the stoichiometric solutions of $Fe(NO)_3{\cdot}9H_2O$ (≥ 99%, Sigma-Aldrich) and $ZrO_2(NO)_2{\cdot}xH_2O$(≥ 99%, Alfa Aesar, x=6) were dissolved in deionized water separately in the mole ratios of 85:15. Then these two solutions were mixed with a cation concentration of 0.1 M in a beaker and polyvinylpyrrolidone (PVP, Sigma-Aldrich) as a surface active agent was added while stirring constantly for 30 min. The mixture solution was then added dropwise to an ammonium carbonate $(NH_4)_2CO_3$ (Sigma Aldrich) solution under constant stirring while maintaining the temperature of the solution to 35°C. To make sure full precipitation of a cation in the solution, the molar ratio of $(NH_4)_2CO_3$ and Mn+ (M=Zr and Fe) was kept as n $(NH_4)_2CO_3$:nM^{n+}=2.5:1. The resultant brownish precipitation was left for 20 h in the solution with continuous stirring. Finally, the suspension was filtered and washed several times with deionized water followed by overnight drying at 80°C. To obtain the precursor Fe_2O_3/ZrO_2, the collected precipitate was calcined at 600°C for 5 h.

Fe_2O_3/ZrO_2-Ir: The prepared Fe_2O_3-ZrO_2 was the first ball milled using planetary ball milled (BM4X-04, COL-INT TECH) in a zirconia container for 20h with 300 rpm speed. Then 0.1 g Ir precursor Iridum III 2,4 pentanedionate ($C_{15}H_{21}IrO_6$, sigma Aldrich) was dissolved in 2 ml acetone (99.5% Sigma Aldrich). Later, the solution was mixed with 1 g of milled Fe_2O_3-ZrO_2 precursor powder in an agate mortar followed by hand grinding. Finally, the obtained powders were calcined at 600°C for 2h.

2.2 Material Characterization

The phase composition of prepared composites Fe_2O_3/ZrO_2 and Ir-added Fe_2O_3/ZrO_2 as well as products of the redox reaction were examined by X-Ray diffraction (XRD, Rigaku D/MAX-2100) at a scan rate of 3°C/min from 20 to 80°. The morphologies of the prepared materials before and after the reaction were also captured by a field emission scanning electron microscope (FESEM, Zeiss Gemini500).

2.3 Kinetics Measurement Setup

To create a similar reaction atmosphere to the battery, the reduction of prepared baseline composites Fe_2O_3-ZrO_2 and Ir-added Fe_2O_3-ZrO_2 material and their respective kinetic studies were performed in a fixed bed reactor; the experimental setup is shown in Figure 1.

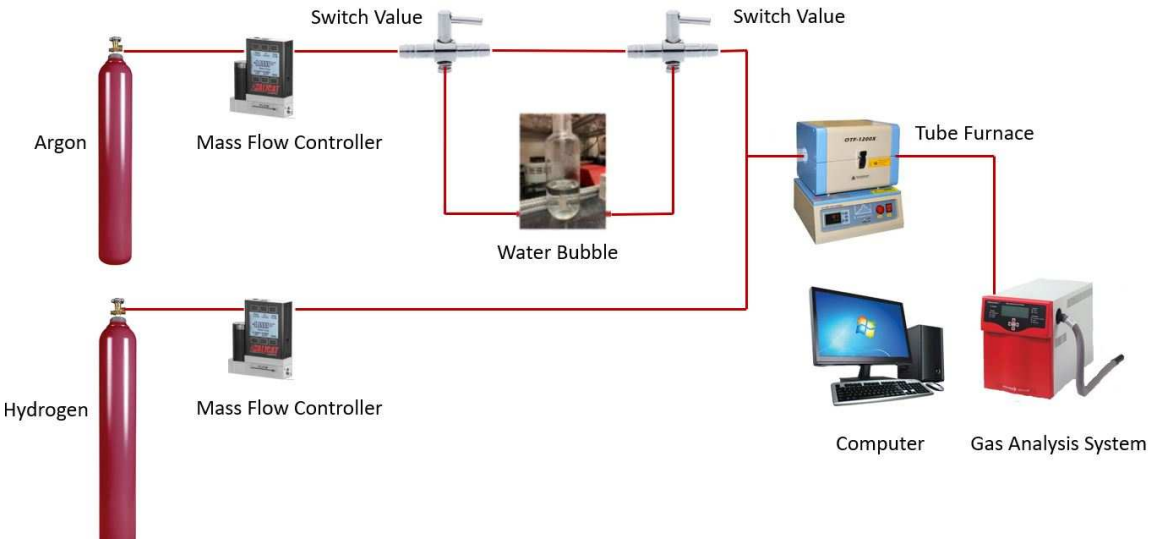

Figure 1. Experimental setup for kinetic study of FeO_x reduction.

The experimental setup mainly consists of a quartz reaction tube, fixed bed, water bubbler, mass flow controllers, switch valve, and mass spectrometer (MS, Pfeiffer Omnistar 100) connected at the outlet of the reactor tube. The steam was controlled by a water bubbler at room temperature which will provide fixed H_2O content to a carrier gas. The gas flow rate was controlled by a mass flow controller (Alicat Scientific MFC Series). MS was used to analyze the effluent compositions and confirm a full reduction of the starting oxide Fe_2O_3 to Fe. The starting oxide composition for reduction process depends on the ratio of partial pressure of H_2O/H_2.

To run the experiment, 100 mg of Ir-added Fe_2O_3/ZrO_2 supported on a lump of quartz wool was first placed inside a quartz glass tube, followed by raising furnace temperature to 400 ^oC with the argon flow rate at 200 cm^3/min. Then 10% H_2-Ar mixture gas was introduced in a reactor during the temperature rise to a target temperature, i.e., 500, 525, 500, 575 ^oC. Mass spectrometer (MS) connected to the tube furnace was used to analyze the outlet gas concentrations during the initial reduction of the Fe_2O_3 into Fe and the degree of the reduction is mainly confirmed by H_2 concentration. Upon full reduction, there will be no H_2 consumption. After this initial reduction activation process with 10% H_2-Ar concentration (total of 100 sccm), the oxidation process was carried out by switching the gas with a controlled H_2O/H_2 ratio to achieve desired oxide form. The starting oxide form for the reduction cycle depends on the temperature and ratio of partial pressure of H_2O and H_2. Therefore, we have chosen H_2O oxidation cycle to create in situ equilibrium Fe oxide composition for the subsequent reduction kinetics study [8].

To control the pressure ratio H_2O/H_2, a fixed flow rate of H_2 was added to a flow rate of moistened Ar steam (100 sccm) at room temperature. For reference, a thermodynamic phase diagram was used to guide the pressure ratio of H_2O/H_2, i.e., for

reduction Fe_3O_4 to Fe at 500-575°C, pH_2O/pH_2 was set to 2. Once desired oxide is obtained, the reduction (Fe_3O_4 to Fe) was carried out in 20% H_2-Ar concentration (total 100 sccm). The reduction kinetics was calculated based on the change in H_2O concentration in the effluent measured by MS. The starting oxide composition for the reduction kinetics study as Fe_3O_4 is confirmed by X-Ray Diffraction.

3. Results and Discussion

3.1 Confirmation of the Starting Oxide for H_2 Reduction

To confirm the starting oxide composition, i.e., Fe_3O_4, after oxidizing Fe by using 3% H_2O mixed with H_2 (Fe was obtained from the initial reduction of Ir-Fe_2O_3/ZrO_2 by H_2), the partial pressure ratio of H_2O and H_2 in equilibrium with the formed Fe_3O_4 was calculated by the measured outlet concentrations of H_2O and H_2 with MS. The thermodynamic phase equilibrium diagram shown in Figure 2 indicates a three-phase domain: Fe, FeO, and Fe_3O_4 [9]. At T<550°C, Fe and Fe_3O_4 are in equilibrium with a pressure ratio of H_2O and H_2 of ~0.8, which means Fe_3O_4 can be directly reduced into Fe in a single step by H_2. On the other hand, at T>600°C, there is an intermediate phase FeO before Fe_3O_4 is reduced to Fe. Therefore, P_{H2O}/P_{H2}=2 is chosen to obtain Fe_3O_4 oxide phase composition for Fe_3O_4 to Fe reduction at T<550°C.

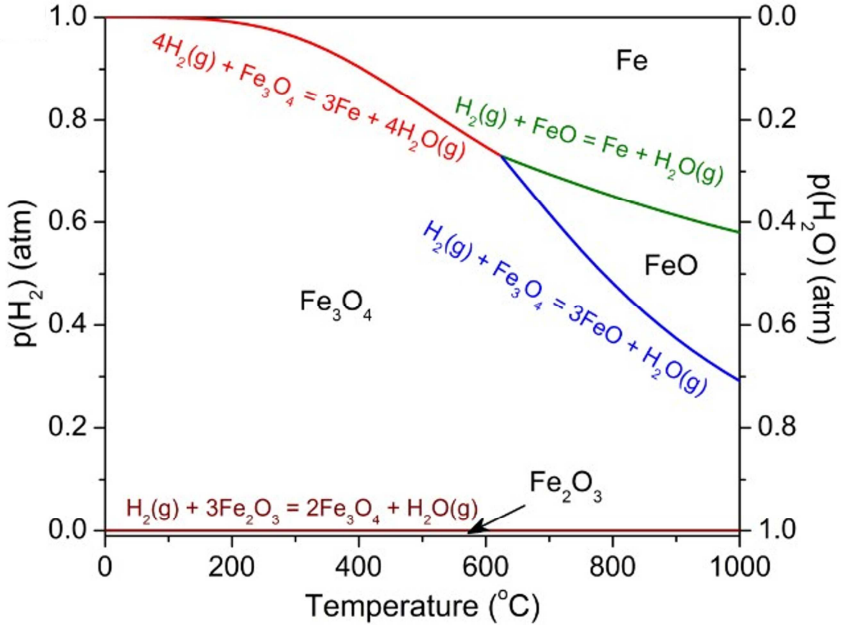

Figure 2.Thermodynamics phase equilibrium a function of temperature and $p(H_2)$ and $p(H_2O)$. [9]

3.2 Phase Composition and Morphologies of Fe Oxides before and after Reduction

The phase compositions of Fe_2O_3-ZrO_2 and Ir-added Fe_2O_3-ZrO_2 composite are confirmed by XRD patterns in Figure 3. The composite powder Fe_2O_3/ZrO_2 shows the peaks at 24, 33.2, 35.6, 40.8, 49.5, 54.1,62.4, 63.98° related to planes (012), (104), (110), (024), (116), (214), (300) of Fe_2O_3 (PDF# 84-0308). These sharp peaks show high crystallinity and purity of sample synthesized by co-precipitation. After introducing IrO_2, a wide peak at 28.1°C appears and can be indexed to the plane (110) of IrO_2. The low

intensity and broader peak of IrO_2 suggest low its crystallinity. Figure 4 shows the phase composition of the material after experiencing the first redox cycle at 500°C. It is evident that all XRD peaks of ZrO_2 remain unchanged even though the peak at 28.2°C is weak due to the high crystallinity and high content of Fe and Fe_2O_3, suggesting its chemical stability to Fe-based materials and H_2**.** Note the initial IrO_2 will become Ir metal at above 200°C.

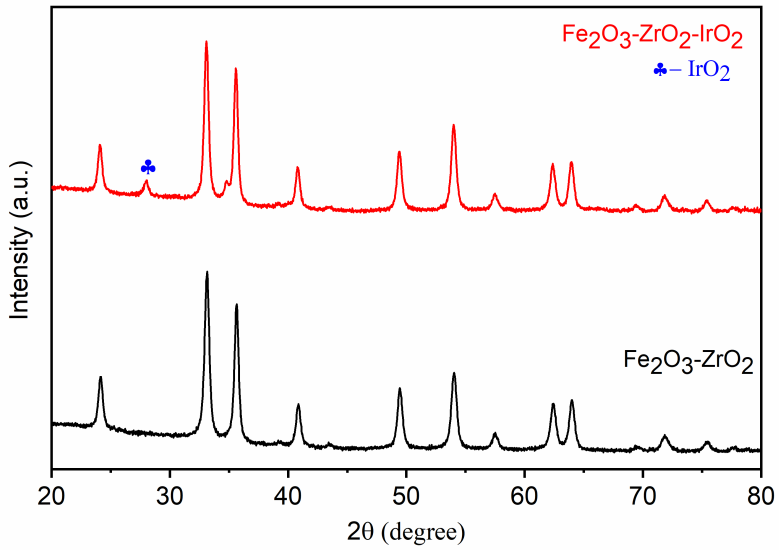

Figure 3. XRD patterns of the baseline Fe_2O_3/ZrO_2 and Ir-added Fe_2O_3/ZrO_2.

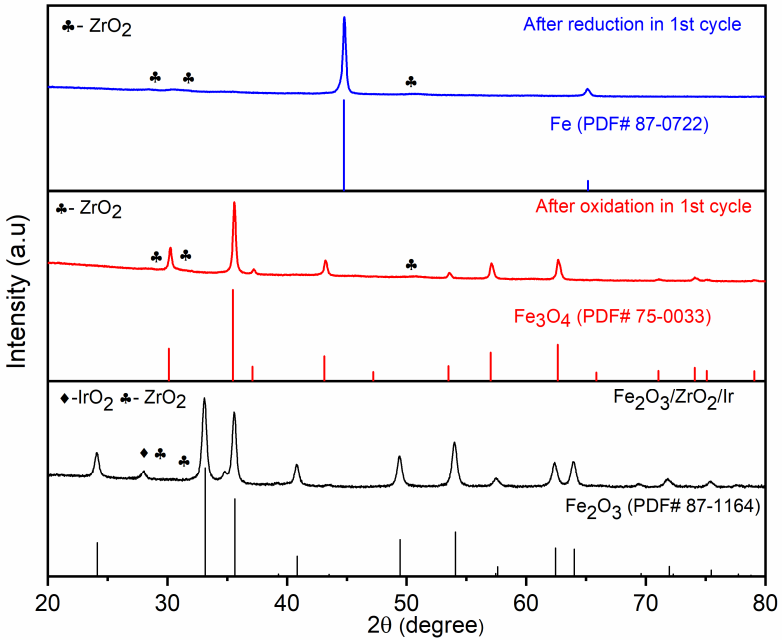

Figure 4. XRD patterns of Ir-added Fe_2O_3/ZrO_2 before and after the 1st redox cycle at 500°C.

The morphologies of Fe_2O_3/ZrO_2-Ir before reduction are shown in Figure 5(a), featuring uniform spherical nanoparticles. After the reduction in 20%H_2, Figure 5(b)-(d), particles are slightly agglomerated and shown with the worst agglomeration at 575 °C , see Figure

5e. But still, there are some nanoparticles seen on the surface of large particles. The elemental mapping of the reduced sample is shown in Figure 5(f1)-(f3), where a uniform distribution of Fe, Zr and Ir elements is observed.

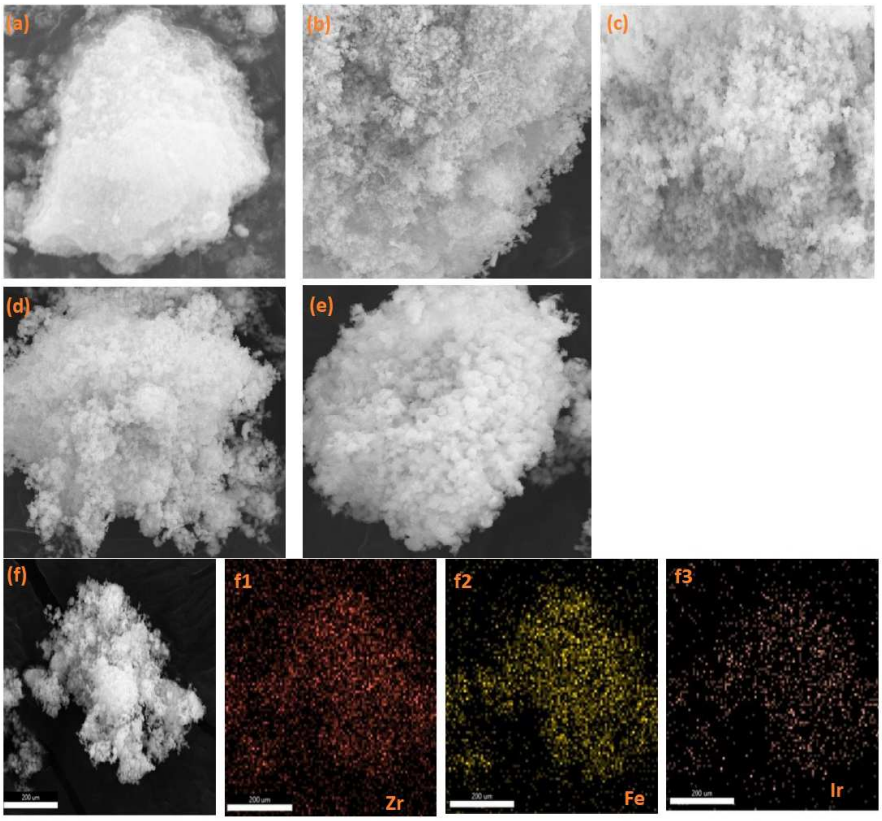

Figure 5. SEM images of powders of (a) fresh Ir-catalyzed Fe_2O_3/ZrO_2 and after reduction in 20% H_2 at (b) 500 (c) 525 (d) 550 and (e) 575 ^oC.

3.3 Reduction Kinetics Modeled by Johnson-Mehl-Avrami Theory

The Johnson-Mehl-Avrami, *aka.* JMA, theory describes isothermal reduction kinetics with solid-state transformation consideration [10-12]. The reduction process of FeO_x by H_2 normally involves a sequence of nucleation and growth steps [7]. The JMA model is related to the reaction fraction (ξ) at constant temperature and reaction time. Referring to [8], the reduction extent (Fe_3O_4-to-Fe) ξ vs. time t is expressed by

$$\xi(t) = \frac{\int_0^t (I_{H2Oprod})dt}{S_{red}} \quad [1]$$

Here, $I_{H2O\,prod}$ is time-dependent ion current of MS related to H_2O production; S_{red} is the peak area of full reduction process.

The kinetic rate constant k(T) is calculated by the following if ξ is known.

$$\xi(t) = 1 - \exp[-k(T)t^n] \quad [2]$$

where k(T) is a rate constant expressed by $k(T) = A * \exp(-\frac{E_a}{RT})$. ξ(t) shows certain kind of topochemical solid-state reaction and is analyzed by the kinetic model proposed by

Avrami and Johnson [13-16]. In this model, a new phase is germ nucleated and distributed throughout the solid, followed by grain growth of an old phase until transformation is completed [10].

Sharp-Hancock equation can be derived by taking logarithmic of eq. (2) to study the order of solid-state reaction [17]**:**

$$\ln[-\ln(1-\xi)] = n\ln(t) + \ln(k) \quad [3]$$

where n is Avrami exponent, which depends on the nucleation and crystal growth of a phase boundary surface [17]. Generally, n= λ+β, where λ is the dimensionality of growth, λ=1, 2 or 3 and β depends on the nucleation process to the overall kinetics (0<β<1, 0 represents instantaneous nucleation and 1 means a very slow nucleation rate) [7]. The valve of n =1-2 signifies to 1D growth, n=2-3 for 2D growth and n=3-4 for 3D growth for each process of a different temperature [10].

The local n(ξ) is calculated by differentiating eq. (3)

$$n(\xi) = \frac{\partial \ln(-\ln(1-\xi))}{\partial \ln(t)} \quad [4]$$

For FeO_x reduction process, the reaction rates can also be expressed by

$$\frac{d\xi}{dt} = k(T) * f(\xi) \quad [5]$$

where f(ξ) is an integral mathematical function depending on kinetic model. For the reduction kinetics under isothermal condition, it can be integrated to yield

$$g(\xi) = \int_0^{\xi} \frac{d\xi}{f(\xi)} = k * t = A * \exp\left(\frac{E_a}{RT}\right) t \quad [6]$$

where g(ξ) is an integral mathematical function related to the mechanism of reduction reaction. Using logarithmic form and rearrangement of eq. (6), we get

$$\ln(t) = (-\ln(A) + \ln\big(g(\xi)\big) + \frac{Ea}{RT} \quad [7]$$

where t is the reaction time corresponding to reduction extent ξ. By plotting ln(t) vs. 1/T, activation energy, E_a, can be obtained at different ξ.

3.4 Modeling Experimental Data

The reduction kinetics of Fe_3O_4 to Fe in H_2 gas environment was evaluated by measuring the change in H_2O concentration in the effluent through MS. The data was processed using the JMA model. During the reduction process, the change in H_2O concentration vs. time is caused by oxygen removal from iron oxide. The outlet H_2O concentration vs. time from 500 to 575 ^oC during reduction process under 20% H_2 is shown in Figure 6. Figure 7 shows the corresponding reduction extent of Fe_3O_4 vs. time.

From Figure 6, the H_2O production is faster in early stage than later stage. The kinetic rate constant is determined by applying JMA model (eq. (1)) to the experimental data, the fitted lines is shown in the Figure 7. All ξ(t) isotherm plots are of sigmoid shape and can be divided into 3 distinct regions: incubation period ($0 < \xi < 0.1$), acceleration regions ($0.1 < \xi < 0.65$) and deceleration region ($0.65 < \xi < 1.0$). It can be observed that with increasing temperature, ξ shows shorter incubation period. The incubation period is dominated by nucleation events, while the acceleratory region can be related to the development of a new phase and the deceleration region corresponds to the termination

of the growth due to the coalescence of Fe particles and thus affects the diffusion [7]. The values of k, n and E_a are calculated from the fitting results and summarized in Table 1. An average value of n =1.08 was obtained. This value indicates the phase transitions continues as a 1D growth process ($\lambda = 1$) with a small nucleation contribution. The activation energy was found to be 44.97 kJ/mol for temperature 500-575 ^{o}C at 20 % H_2, see Figure 8.

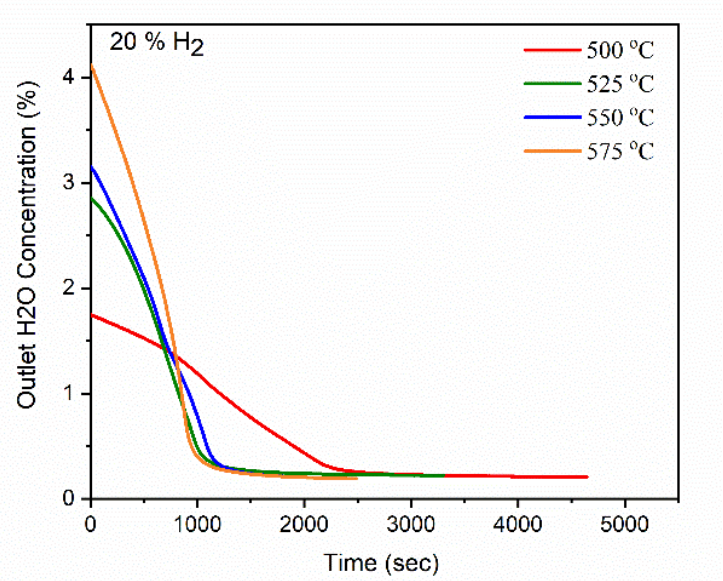

Figure 6. Profile of outlet water concentration during reduction process in 20% H_2-Ar at 500 to 575 ^{o}C.

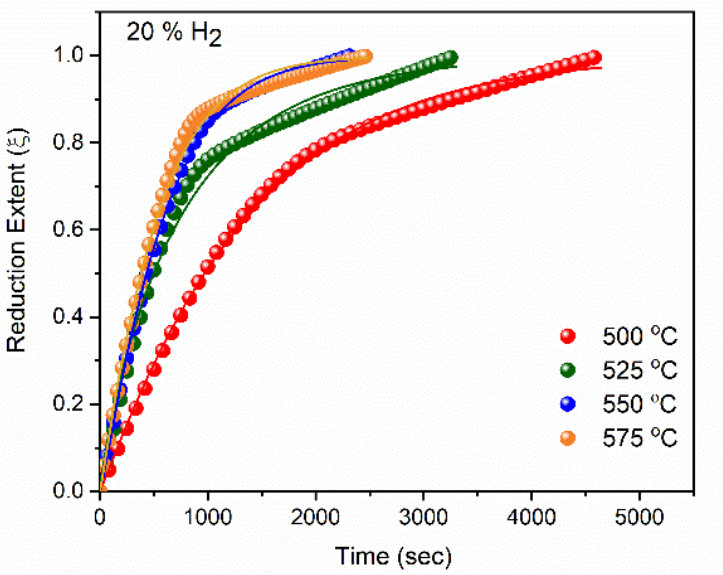

Figure 7. Reduction extent profile of Fe_3O_4 vs. time and JMA model fitting curves at 500-575 ^{o}C.

The Sharp and Hancock eq. (3) is used to evaluate the order of solid-state reaction rate and the plots of ln(-ln(1- ξ)) vs. ln(t) is based on the experimental data at 500-575^{o}C at 20% H_2-Ar; the results are shown in the Figure 9. It shows 3 distinct stages with different Avrami exponent (n) in the whole conversion process. It can be clearly seen that when reduction extent is close to 1, n tends to be infinite (ξ ≠ 1 boundary condition for

eq. (3)). The variation of local exponent with reduction extent implies the different dominating mechanism in each stage of reaction [7] and are also plotted Figure 10.

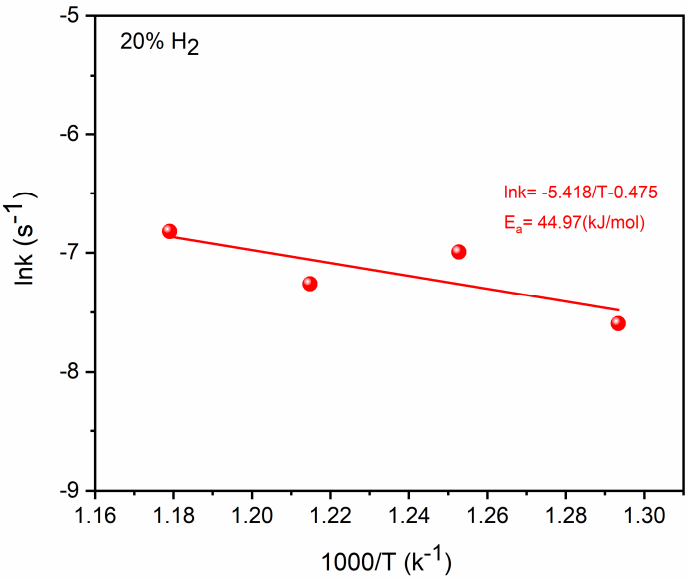

Figure 8. Arrhenius plot of rate constant of Fe_3O_4 to Fe reduction extracted from JMA model.

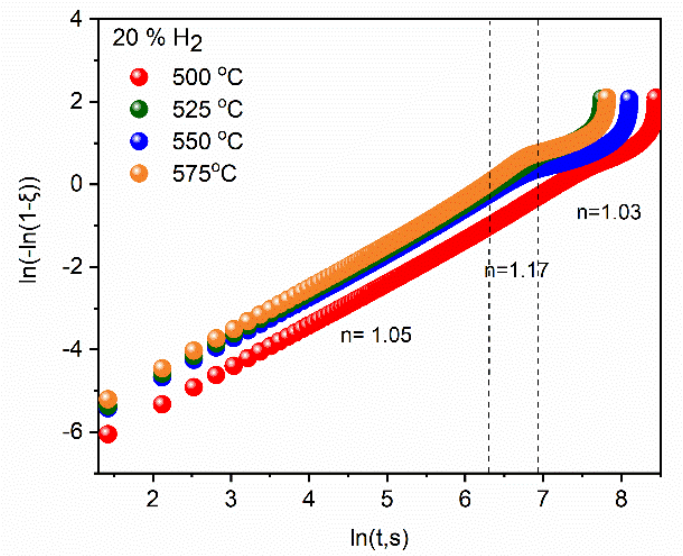

Figure 9. Sharp-Hancock plots based on the data at 500-575°C in 20% H_2.

At the beginning of reaction, n slowly increases and reaches a maximum value, indicating 1D growth with decreasing nucleation rate, which agrees well with Figure 10. At end of the reaction, n tends to fall below 1, implying slower diffusion due to sintering of Fe particles. To get the clear idea of mechanism, we plotted eq. (7), ln(t) vs. 1/T in figure 11 at ξ =0.05 -1, from 500-575°C in 20% H_2. For a given ξ, E_a is calculated from the slope of each line and shown in Figure 12. In this case with increasing ξ, E_a first increases from 53.39 to 55.6 kJ/mol within $0.05 < \xi < 0.15$, then very slowly increases to 60.38 kJ/mol within $0.15 < \xi < 0.7$ and then increases again to 78.54 kJ/mol for $0.75 < \xi < 0.85$, and finally decreases to 57.22 kJ/mol at the end of reduction. This

variation indicates the changes in growth and nucleation mechanism during reduction process.

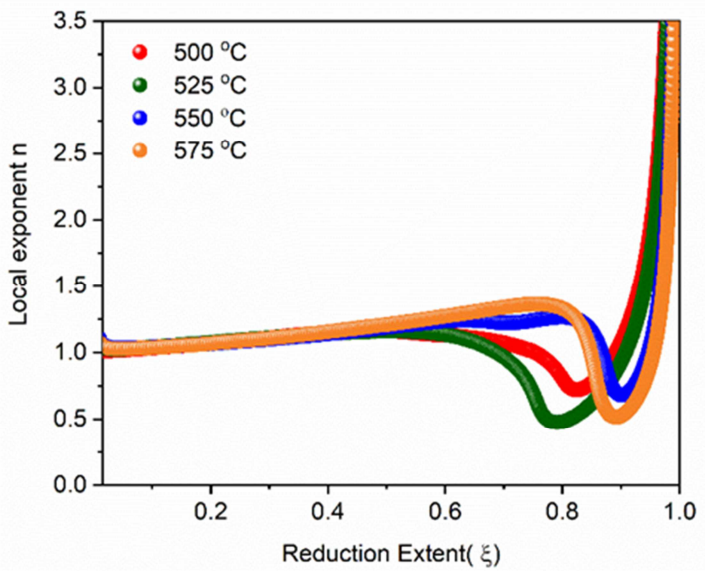

Figure 10. Local exponent n values vs. ξ at 500-575°C in 20% H_2.

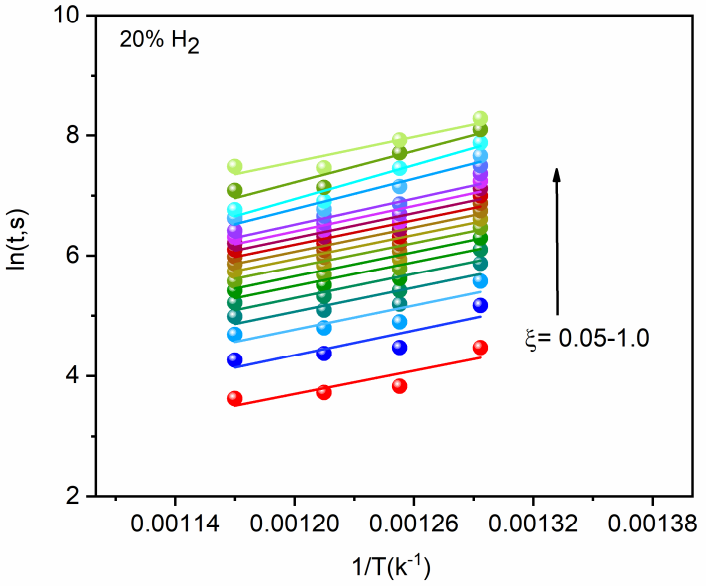

Figure 11. ln(t) vs.1/T with ξat 500-575°C in 20% H_2.

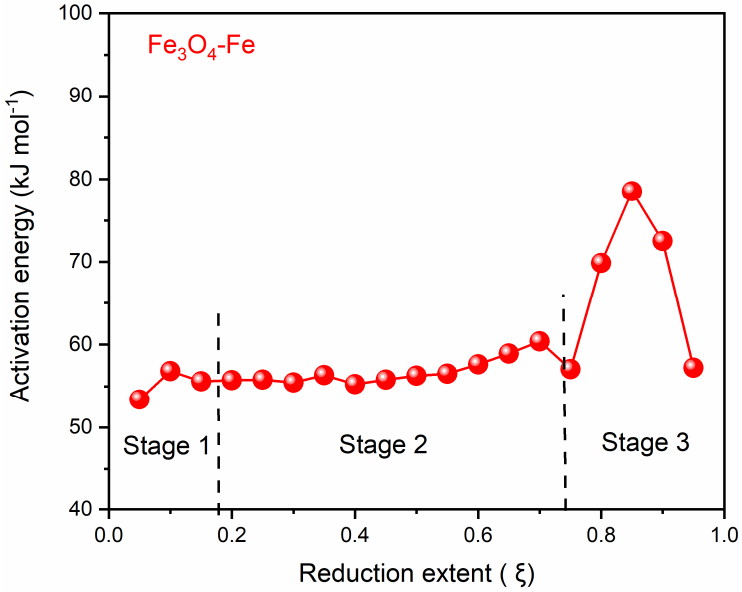

Figure 12. E_a vs. ξ for Fe_3O_4 to Fe conversion.

3.5 Comparison of Reduction Kinetics between Baseline and Ir-added Fe_2O_3/ZrO_2

The kinetics of baseline material Fe_2O_3-ZrO_2 and Ir-added Fe_2O_3-ZrO_2 are compared in Figure 13. It is evident that Ir significantly boosts the reduction kinetics of FeO_x. The E_a of both materials is calculated and indicated in the Figure 13. Since E_a for Ir-added Fe_2O_3/ZrO_2 is slightly higher (44.97 kJ/mol) than baseline material (40.13 kJ/mol), the high pre-exponential factor (A) must be the reason for the boosted kinetics, see Figure 13. From Figure 14, we can find that E_a of the baseline material decreases with ξ, implying that E_a of nucleation is higher than growth of new phase, which means it follows nucleation and growth model. In contrast, E_a slowly increases with ξ up to 0.7 and then decreases at the end for Ir-added Fe_2O_3/ZrO_2. In addition, at the end of a reduction period, there might be possibility of densification of Fe-particles, resulting in higher E_a. Compared to the Fe_2O_3/ZrO_2 reduction, the kinetic rate constant of Ir-added Fe_2O_3/ZrO_2 is one order of magnitude higher. The values of n and E_a of both materials are summarized in the Table1.

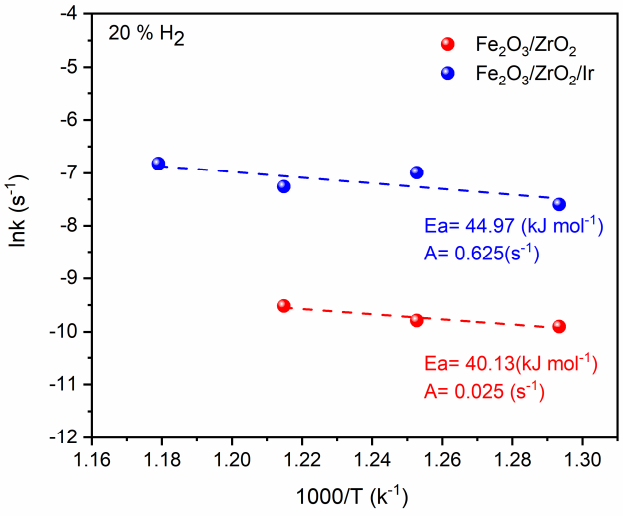

Figure13. Comparison of E_a of Fe_2O_3/ZrO_2 with Ir-catalyzed Fe_2O_3/ZrO_2.

Table 1. Summary of fitting results of Fe_3O_4 using JMA model

	Fe_2O_3/ZrO_2			Fe_2O_3/ZrO_2 - Ir			
T(^{o} C)	500	525	550	500	525	550	575
k(s^{-1})	$5.01*10^{-5}$	$5.62*10^{-5}$	$7.37*10^{-5}$	$5.024*10^{-4}$	$9.17*10^{-4}$	$7.029*10^{-4}$	$1.09*10^{-3}$
n	1.45	1.45	1.45	1.08	1.08	1.08	1.08
R^2	0.999	0.995	0.998	0.997	0.98	0.99	0.99
E_a (kJ mol^{-1})	40.1± 2.3			44.5			

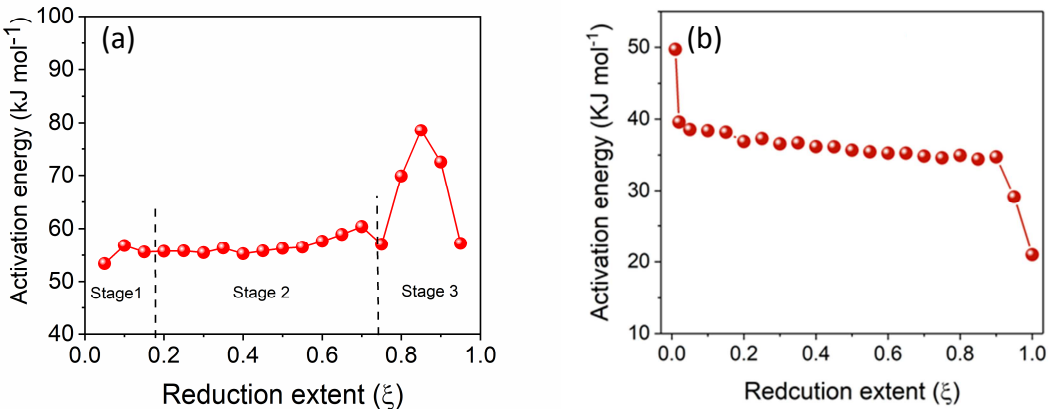

Figure 14. E_a vs. ξ of (a) Ir-added Fe_2O_3/ZrO_2 and (b) baseline Fe_2O_3/ZrO_2 [7].

4. Conclusion

The reduction kinetics study of Ir-added Fe_2O_3/ZrO_2 was carried out in 20% H_2 in 500-575 ^{o}C by MS. The desired starting iron oxide, Fe_3O_4, was obtained by controlling the ratio of H_2O and H_2 concentration. The reduction kinetics of Fe_3O_4 to Fe was modeled by Johnson-Mehl-Avrami (JMA) theory. The obtained rate constant of Ir-added Fe_2O_3/ZrO_2 is one order magnitude higher than Fe_2O_3/ZrO_2. The increased rate constant was found to result from the high pre-exponential factor (A), not the activation energy. The variations in E_a follows three steps involving the change in nucleation and growth.

Acknowledgements

We would like to thank National Science Foundation for the financial support under award no. 1801284.

References

[1] C. Zhang and K. Huang, ACS Energy Letters, 1(6), 1206–1211 (2016).

[2] X. Zhao, X. Li, Y. Gong, N. Xu and K. Huang, RSC Adv., 4(43), 22621–22624 (2014).

[3] X. Zhao, X. Li, Y. Gong and K. Huang, Chemical Communications, 50(5), 623–625 (2014).

[4] X. Zhao, Y. Gong, X. Li, N. Xu and K. Huang, Journal of The Electrochemical Society, 160(10), A1241-A1247 (2013).

[5] X. Jin, X. Zhao and K. Huang, Journal of Power Sources, 280, 195-204 (2015).

[6] Tang Q, Zhang Y, Xu N, Lei X, Huang K. Energy & Environmental Science, 15(11), 4659-71 (2022).

[7] Tang Q, Huang K. Chemical Engineering Journal, 434(C) (2022).

[8] Tang Q, Ma Y, Huang K. ACS Applied Energy Materials, 15, 4(7) (2021).

[9] Zhang C, Huang K. In Solid Oxide-Based Electrochemical Devices, pp. 217-250 Academic Press (2020).

[10] Piotrowski K, Mondal K, Wiltowski T, Dydo P, Rizeg G.. Chemical Engineering Journal, 131(1-3), 73-82 (2007).

[11] C.E. Seaton, J.S. Foster, J. Velasco. Transactions of the Iron and Steel Institute of Japan, 23 (6), 490–496 (1983).

[12] S.S. Jung, J.S. Lee. Mater. Transactions, 50, 2270–2276 (2009).

[13] Avrami M. J Chems. Phys., 7, p.1103-12 (1939).

[14] Avrami M. J Chems. Phys., 8, p. 212 (1940).

[15] Avrami M. Granulation, J Chem. Phys., 9, p. 177 (1941).

[16] Erofe'ev BV. Compt Rend Acad Sci USSR, 52, p. 511-4 (1946).

[17] Monazam, E. R.; Breault, R. W.; Siriwardane, R. Energy Fuels, 28, 5406−5414 (2014).

[18] Zhang C, Huang K. Advanced Energy Materials, 11(2), 2000630 (2021).